

Water Resources Research

RESEARCH ARTICLE

10.1029/2019WR024898

Special Section:

Advances in remote sensing, measurement, and simulation of seasonal snow

Key Points:

- Extensive ground observations show that airborne lidar data accurately captured snow depth patterns underneath forest canopies
- A continuous measure of local distance to canopy edge (DCE) was developed to derive new canopy and gap size distribution parameters
- DCE-based canopy metrics were successful in describing snow distribution characteristics across a range of spatial scales (1–200 m)

Supporting Information:

- Supporting Information S1

Correspondence to:

G. Mazzotti,
giulia.mazzotti@slf.ch

Citation:

Mazzotti, G., Currier, W. R., Deems, J. S., Pflug, J. M., Lundquist, J. D., & Jonas, T. (2019). Revisiting snow cover variability and canopy structure within forest stands: Insights from airborne lidar data. *Water Resources Research*, 55. <https://doi.org/10.1029/2019WR024898>

Received 31 JAN 2019

Accepted 10 JUL 2019

Accepted article online 16 JUL 2019

Revisiting Snow Cover Variability and Canopy Structure Within Forest Stands: Insights From Airborne Lidar Data

Giulia Mazzotti^{1,2} , William Ryan Currier³ , Jeffrey S. Deems⁴ , Justin M. Pflug³ , Jessica D. Lundquist³ , and Tobias Jonas¹ 

¹WSL Swiss Federal Institute for Snow and Avalanche Research, Davos, Switzerland, ²Laboratory of Hydraulics, Hydrology and Glaciology, ETH Zurich, Zurich, Switzerland, ³Department of Civil and Environmental Engineering, University of Washington, Seattle, WA, USA, ⁴National Snow and Ice Data Centre, Boulder, CO, USA

Abstract The retrieval of detailed, co-located snow depth and canopy cover information from airborne lidar has advanced our understanding of links between forest snow distribution and canopy structure. In this study, we present two recent high-resolution (1 m) lidar data sets acquired in (i) a 2017 mission in the Eastern Swiss Alps and (ii) NASA's 2017 SnowEx field campaign at Grand Mesa, Colorado. Validation of derived snow depth maps against extensive manual measurements revealed a RMSE of 6 and 3 cm for plot-level mean and standard deviation of snow depth, respectively, demonstrating that within-stand snow distribution patterns were captured reliably. Lidar data were further processed to obtain canopy structure metrics. To this end, we developed a novel approach involving a continuous measure of local distance to canopy edge (DCE), which enabled creating spatially aggregated nondirectional and directional descriptors of the canopy structure. DCE-based canopy metrics were correlated to mean and standard deviation of snow depth over areas representing grid-cell sizes typical of watershed and regional model applications (20–200 m). Snow depth increased along the DCE gradient from dense canopy to the center of canopy gaps for all sites and acquisition times, while directional effects particularly evolved during the ablation season. These findings highlight the control of canopy gap distribution on snow distribution in discontinuous forests, with higher snow depths where the open fraction is concentrated in few large gaps rather than many fragmented small gaps. In these environments, dedicated canopy structure metrics such as DCE should advance spatially distributed snow modeling.

1. Introduction

In forested areas, snow distribution dynamics are shaped by complex interacting processes such as snow interception (Moeser, Stähli, et al., 2016; Storck et al., 2002), shading from solar radiation (Musselman et al., 2015) and enhanced longwave irradiance (Sicart et al., 2006; Webster et al., 2016), which create pronounced variability at small spatial scales. The nonuniform snowpack develops into a fractional snow cover in springtime, modulating magnitude and timing of streamflow and altering radiative and turbulent energy fluxes between the land surface and the atmosphere (Liston, 1999). Understanding and quantifying the control of forest architecture on snow distribution is important, as forests are subject to changes due to clearcutting and timber harvesting (Ellis et al., 2013; Murray & Buttle, 2003; Troendle & King, 1987), wildfires (Burles & Boon, 2011; Harpold, Biederman et al., 2014), and mortality caused by insect infestation (Biederman et al., 2014; Winkler et al., 2014). These shifts affect snow cover dynamics and, given the large spatial overlap of forests and seasonal snow, further impact hydrological regimes and the climate system (Rutter et al., 2009).

The interplay of localized processes can be represented explicitly in high-resolution (~1 m) models (Broxton et al., 2015; Moeser, Mazzotti, et al., 2016) but constitutes a major challenge especially at coarser resolutions, where current model deficiencies have been attributed to the simplified implementation of the canopy (Broxton et al., 2015; Essery et al., 2009). While it is commonly treated as a homogeneous medium characterized by bulk properties (Best et al., 2011; Bonan et al., 2018; Boone et al., 2017), in reality forests consist of a mosaic of trees and canopy gaps. In applications that require a coarser resolution, variability resulting from canopy-induced processes needs to be treated at the subgrid level (Clark et al., 2011). Existing approaches to represent within-cell variability such as tiling (Andreadis et al., 2009; Bartlett

et al., 2006) and probability distribution functions (Essery & Pomeroy, 2004; Liston, 2004; Luce & Tarboton, 2004) currently do not incorporate canopy metrics that reflect its true structural heterogeneity. They may hence not accurately represent the canopy's influence on snow distribution within a forest stand. However, forest snow processes are key drivers of subgrid variability at model scales ranging up to a few hundreds of meters (Clark et al., 2011; Deems et al., 2006; Trujillo et al., 2007). It is therefore important to identify canopy structure parameters that better describe forest snow processes and to integrate these in the aforementioned coarse-scale modeling approaches.

To date, efforts to test and improve coarse resolution forest snow models have been hampered by the limited availability of spatially distributed, comprehensive high-quality data sets (Essery et al., 2009; Jost et al., 2007). Relating forest snow distribution to canopy characteristics has been the subject of a myriad of in situ experimental studies, many of which are outlined in two extensive reviews (Clark et al., 2011; Varhola et al., 2010). Despite the enormous effort associated with data collection, the ability to capture representative snow depth patterns that accurately reflect grid-cell averages and subgrid variability in forested environments has suffered from the poor extent and limited support of these measurements (Bloeschl, 1999; Pomeroy et al., 2002; Winkler & Moore, 2006). In contrast, validation efforts that use satellite products to evaluate large-scale land surface models have strong limitations in forested environments (Toure et al., 2018). Consequently, identifying grid-cell-scale canopy structure metrics that can act as predictors of snow depth averages and variability remains a major challenge (Friesen et al., 2015).

Differential airborne lidar (or Airborne Laser Scanning (ALS)) mapping offers an opportunity to overcome the constraints mentioned above by providing spatial data of both snow distribution and canopy structure at high resolution across previously unavailable extents. However, while the technology is advancing our understanding of spatial snow cover dynamics (Deems et al., 2013; Harpold et al., 2015), forested environments pose major challenges to data acquisition due to the partial obstruction of the signal by trees (Bhardwaj et al., 2016; Nolin, 2010). Therefore, lidar-based studies concerned with forest snow have reported considerable data gaps in subcanopy areas (Broxton et al., 2015; Currier & Lundquist, 2018; Zheng et al., 2016). Existing validation studies have come to contrasting conclusions regarding the performance of lidar in forests, reporting both equivalent (Currier et al., 2019; Hodgson et al., 2005; Reutebuch et al., 2003) and decreased data quality (Hopkinson et al., 2004; Tinkham et al., 2014) compared to nonforested areas. The diversity of these results is partially due to differences in lidar survey parameters, reflecting a trade-off between wide-area and high-resolution mapping (Deems et al., 2013). Accuracy has been also related to parameters describing canopy and understory vegetation (Hopkinson et al., 2004; Tinkham et al., 2014), and difficulties in acquiring accurately geolocated validation data within forest stands have been highlighted (Hopkinson et al., 2012). Whether ALS-based snow depth maps realistically represent forest snow patterns still needs to be assessed (Currier et al., 2019; Harpold, Gou et al., 2014).

In this study, we explore the links between snow depth and canopy structure within forest stands based on recent high-resolution (1 m) airborne lidar data sets from the Swiss Alps and Grand Mesa in Colorado with the following specific objectives:

1. Use new, comprehensive validation data to demonstrate the capability of airborne lidar to reliably capture within-forest snow distribution patterns;
2. Introduce a novel and computationally efficient approach that characterizes the spatial layout of the canopy using nondirectional or directional local measures of DCE;
3. Apply the DCE approach to create spatially aggregated canopy structure descriptors;
4. Identify relationships between snow and canopy distribution, both at the pixel level (1 m) and across a range of spatial scales (20–200 m).

2. Study Areas and Data

2.1. Eastern Swiss Alps

The core data set of this study encompasses two forested study areas in the Grisons region in Switzerland, one on Wolfgang Pass near the town of Davos and the other in the central Engadine valley (Figures 1a, 1d, and 1e). Each site constitutes an area of approximately 0.5 km² within the flight perimeter of a pilot mission from NASA's Airborne Snow Observatory (ASO; Painter et al., 2016) in the Eastern Swiss Alps. The two

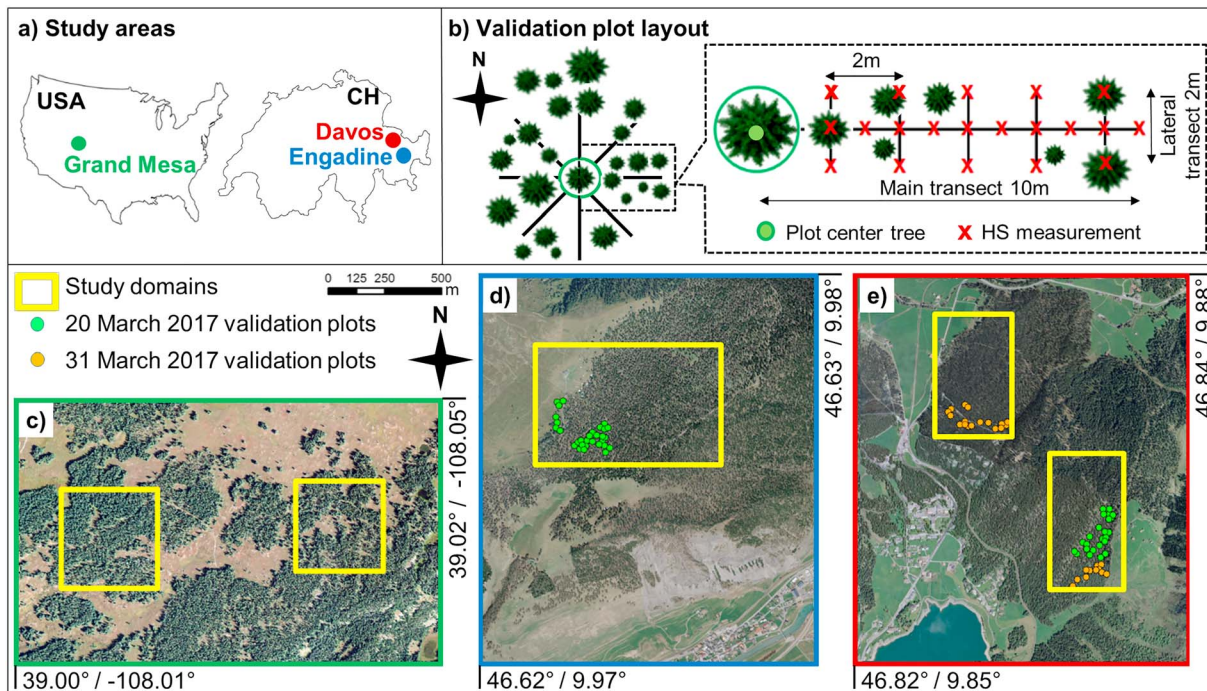


Figure 1. (a) Locations of the American and Swiss study areas. (b) Design of validation plots surveyed within the Swiss forest sites. Aerial image and perimeter of (c) the Grand Mesa sites, (d) the Engadine field area, and (e) the Davos area, both including the location of validation plots.

sites, located at approximately 46.6–46.8° latitude and 1,700 and 2,000 m above sea level, respectively, experience distinctly different weather patterns (e.g., precipitation events) and are therefore treated separately. The locations were selected based on their accessibility, the relatively flat slope, and species composition representative of typical alpine conifer forests. While the Davos forest includes mainly Norwegian spruce (*Picea abies*) and pine (*Pinus sylvestris*), the Engadine site features mostly spruce and larches (*Larix decidua*). Within-site topographic variability, understory growth and ground roughness are limited in the Engadine site but are more pronounced in the Davos forest.

Snow-on ALS data were acquired on three days during the 2017 ablation season (20 March, 31 March, 17 May), the snow-off flight occurred on 29 August of the same year. The target area was covered by overlapping flight stripes at a flight altitude of 4,000 m above sea level, leading to high point densities between 5 and 30 points/m² in the areas of interest. The setup included a Riegl Q-1560 ALS scanning at a 800-kHz pulse rate with a 60° scan angle, which corresponds to ASO's operational configuration (Painter et al., 2016). Flights started after the onset of snowmelt; by 17 May most of the forested areas were snow free.

Manual validation measurements were collected after the two flights in March within 24 hr of the ALS acquisition. Validation plots comprised manual snow probing along eight transects centered around a geolocated tree, designed to capture spatial snow patterns (Figure 1b). Accurate manual georeferencing of the measurements was ensured by selecting center trees that could be identified unequivocally on an aerial image and an existing lidar-based canopy height model, allowing a geolocation accuracy within 1 m. Measurements were taken with 1-m spacing and additionally at each side of the transect every 2 m, on 10-m transects in cardinal and 6-m transects in ordinal directions, resulting in 132 measurements per plot on a 20-m² area. Overall, we surveyed 54 plots at both sites during the 20 March flight (Figures 1d and 1e). As most of the snowpack was depleted in the Engadine by 31 March, validation measurements were limited to the Davos area but were more widespread and included 28 additional plots (Figure 1e). These efforts generated a validation data set consisting of more than 11,000 manual measurements.

2.2. Grand Mesa, Colorado

We complement the Swiss data set with ALS data acquired by ASO during NASA's 2017 SnowEx campaign (Kim et al., 2017) on Grand Mesa, CO, at about 3,200 m above sea level (Figures 1a and 1c), deploying the

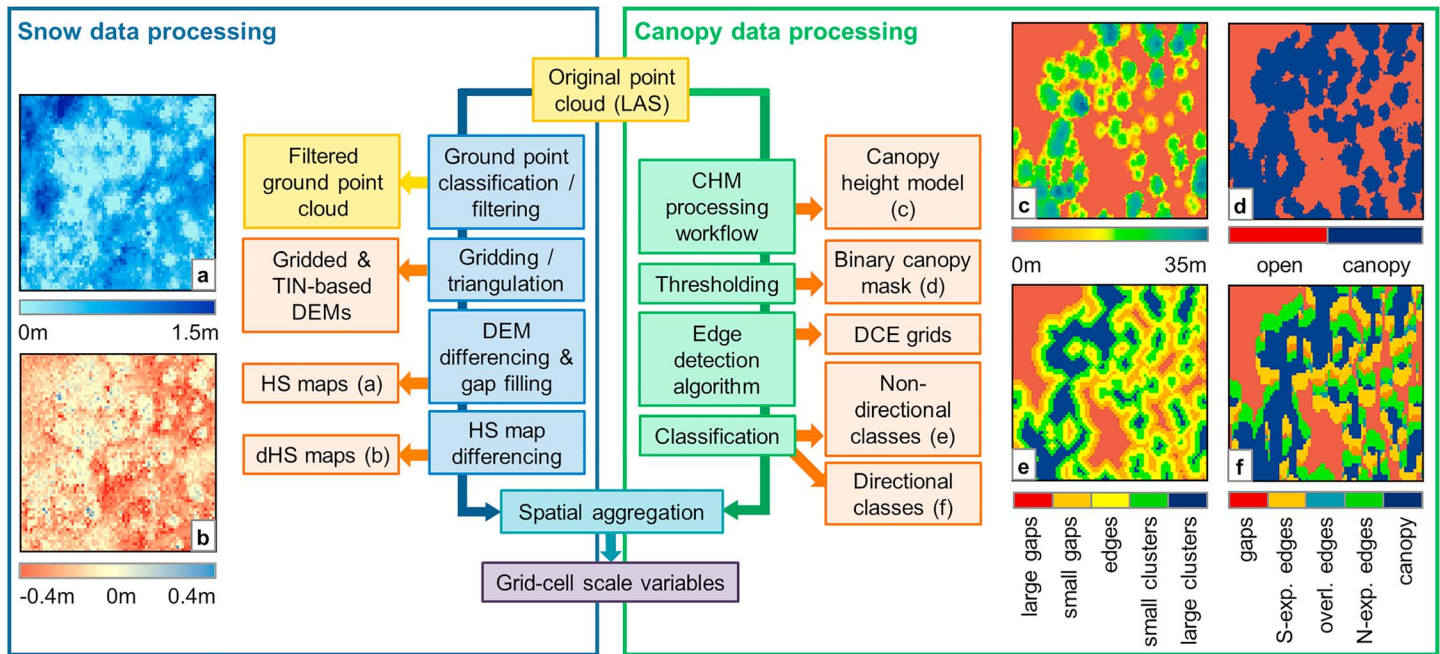


Figure 2. Processing workflow to convert the point cloud data sets (yellow boxes) to 1-m grids (red boxes) and aggregated data sets (purple box), comprising snow data (blue frame) and canopy data (green frame) processing branches. Snow data processing resulted in (a) snow depth and (b) differential snow depth grids. Canopy data processing yielded a (c) canopy height model which was (d) binarized and processed further to compute (e) a nondirectional and (f) a directional canopy classification (DCE-algorithm; cf. section 4.2). The examples of the gridded data sets represent a 70×70 -m area.

same instrumentation but flying at lower altitude (approximately 1,500 above terrain). This allows our analysis to be transferred to a continental, lower latitude (39.0°) site. We selected areas within a discontinuous forest stand with an equivalent extent to the Swiss sites (0.5 km^2 in total), but with substantially flatter topography, less ground roughness, and less understory vegetation. In contrast to the ablation period observed at the Swiss sites, the Grand Mesa data set was collected during the accumulation period and captured a precipitation event of about 15 cm between snow-on flights on 8 and 16 February. Snow depths were 1.5 m on average, in contrast to the 0.5-m mean snow depth in the Swiss data set. The snow-off flight occurred on 26 September 2016. In situ data from Grand Mesa are not considered in this study, but have been compared to the same ALS data sets by Currier et al. (2019).

3. Methods

3.1. Snow Depth Data Processing

Point clouds generated from the full waveform data by standard ASO procedures (Painter et al., 2016) were further processed primarily using lastools software (<http://rapidlasso.com/lastools/>), applying the workflow illustrated in Figure 2. Following Currier et al. (2019), ground points were classified with the lasground tool, using a step size of 2 m and considering last returns only. Ground-classified points were then filtered to include only the lowest 40th percentile of points within each 1-m bounding box, aiming at excluding low-vegetation points wrongly classified as ground. To arrive at a gap-free digital elevation model, these ground points were first gridded using the lasgrid tool, and further converted to a triangulated irregular network (TIN, las2dem tool). The TIN was then used to fill the gaps in the gridded digital elevation model where ground returns could not be retrieved. Snow depth (HS) maps at 1-m resolution were created by digital elevation model differencing, accounting for offsets determined from snow-free areas and restricting the value range to 0–3 m to exclude (rare) obvious outliers that may occur around trees (Figure 2a). Further differencing of the snow depth maps yielded the change in snow depth between the two flights, differential snow depth (dHS; Figure 2b).

3.2. Canopy Structure Metrics and DCE Algorithm

A series of canopy structure descriptors were retrieved from the snow-off scans. Canopy height models at 1-m resolution (Figure 2c) were created following the workflow presented by Khosravipour et al. (2014). A

Table 1
Overview of Pixel Classifications

Pixel classifications	Data basis	Category denomination	Category definition
Binary	Canopy height model (CHM)	Canopy (C)	$CH > 2$
		Open (O)	$CH \leq 2$
Nondirectional DCE classes	DCE grid	Large gaps (D1)	$3 < DCE \leq 8$
		Small gaps (D2)	$1 < DCE \leq 3$
		Edges (D3)	$-1 \leq DCE \leq 1$
		Small clusters (D4)	$-3 \leq DCE < -1$
		Large clusters (D5)	$DCE < -3$
Directional DCE classes	South and north facing DCE grids	South exposed edge (S)	$-3 \leq \text{south DCE} \leq 3$
		North exposed edge (N)	$-3 \leq \text{north DCE} \leq 3$

Refer to Table S1 in the supporting information for further details on the directional distance to canopy edge (DCE) classes not shown in this table. (Thresholds Indicated in Meters).

binary canopy mask was derived from the canopy height models to discriminate between (under-) canopy and open (outside-canopy) pixels based on a 2-m height threshold (Figure 2d), which is consistent with recent literature (Broxton et al., 2015; Currier & Lundquist, 2018; Tennant et al., 2017).

A novel algorithm was developed to characterize canopy distribution. In essence, our approach includes an edge-detection routine run on the binary canopy map, where the pixels adjacent to the canopy edge are tagged and the process iterated to detect cells a step further away from the canopy edge. The resulting aggregated map values indicate each pixel's distance from the canopy edge (DCE), a metric which is further used to define five classes representing different regions within the forest stand (Figure 2e and Table 1). A schematic of the algorithm is shown in Figure 3. The binary canopy raster, where $B = 1$ indicates canopy and $B = 0$ indicates open, is smoothed by applying a symmetric two-dimensional moving average filter with a 3×3 -m window. The smoothed grid serves to identify pixels at the transition from canopy to open pixels (i.e., where $0 < S < 1$). Overlaying the original binary grid with the smoothed grid allows further distinguishing between transition pixels under canopy and transition pixels in the open. In an overlay grid X , defined as $X_o = \max(B, S)$, all pixels with $0 < X_o < 1$ correspond to transition pixels in the open, while in an overlay grid defined as $X_c = \min(B, S)$, pixels with $0 < X_c < 1$ correspond to transition pixels under canopy. These transition pixels are assigned a DCE value of 1 (open) and -1 (canopy) respectively.

The two overlay grids are binarized applying $X_o (X_o > 0) = 1$ in the former and $X_c (X_c < 1) = 0$ in the latter case, to provide the starting points of the next smoothing iteration. From this point onward, two separate iterative loops identify pixels gradually moving away from the original canopy edge: outward in the case of open pixels (red loop in Figure 3) and inward in case of below-canopy pixels (blue loop). The DCE value corresponding to the iteration number N is assigned to pixels delineated at each step, with positive values for open pixels and negative values for below-canopy pixels. Ultimately, the resulting DCE score reflects a signed two-dimensional distance from the canopy edge. Further information, including the algorithm code, is provided in the supporting information.

Pixels were also classified based on their DCE. The DCE thresholds defining the classes, reported in Table 1, were motivated by results presented in section 5.2. As these classes are based on location relative to the canopy edge, they can be thought of as large (D1) and small (D2) gaps, the canopy edge region (D3), small (D4) and large (D5) canopy clusters (Figure 2e and Table 1).

A similar approach based on the same concept was further implemented to derive an alternative pixel classification, which additionally accounts for edge orientation. In this case, asymmetric two-dimensional forward-moving average filters pointing southward and northward, respectively, were applied separately to the binary canopy mask, to derive distance to the south and north exposed canopy edge. This allowed pixels to be classified into open and canopy pixels, south facing and north facing edges (Figure 2f). Note that some pixels fulfilled the criteria for both north and south facing canopy edges; these were tagged as overlapping edges (Table 1). An application example of the directional DCE algorithm illustrating the first three iteration steps is included in Text S1 and Figure S2 in the supporting information.

3.3. Validation of ALS-Based Snow Maps

Individual manual measurements around each intersection point (of main transects and lateral measurements; see Figure 1b and column "Manual HS measurements" in Figure 5) were aggregated to obtain 32

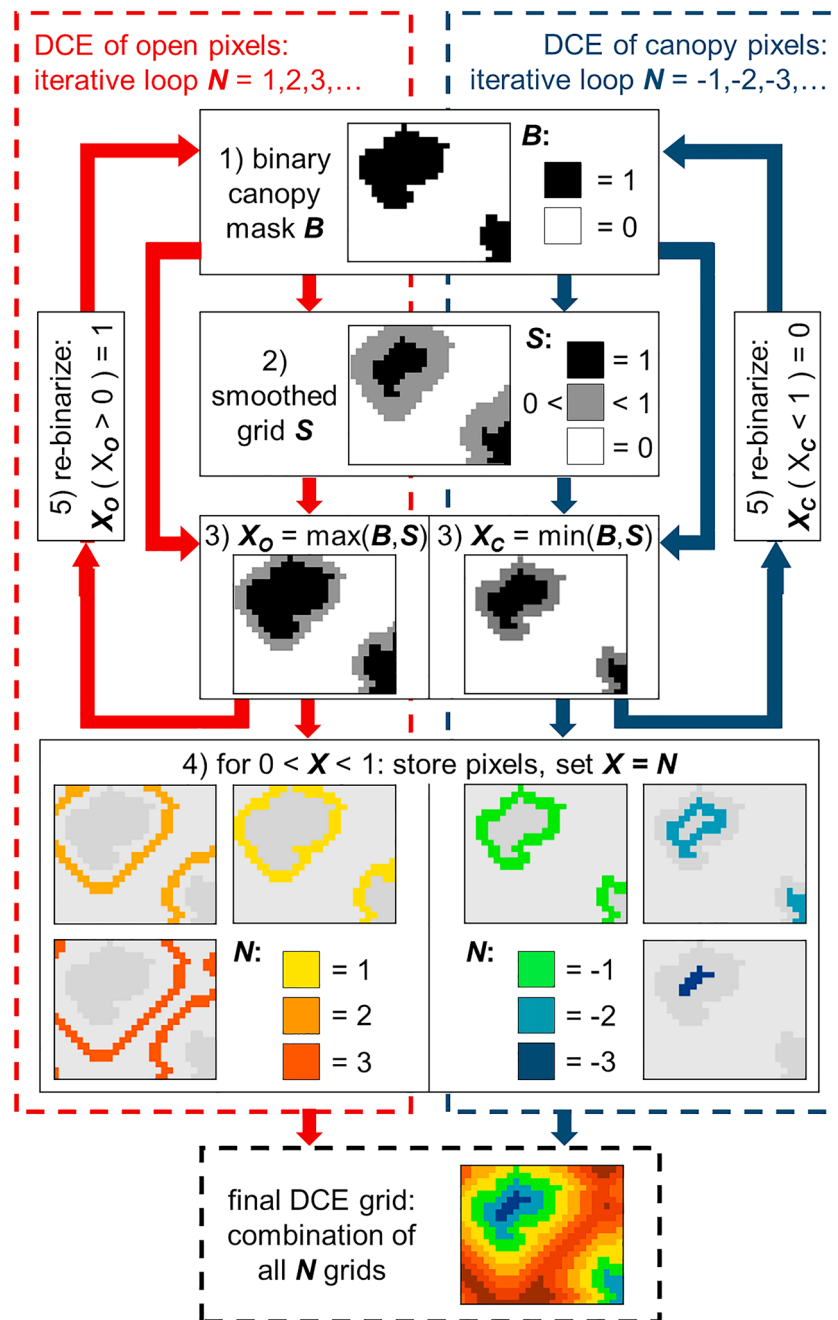


Figure 3. Conceptual schematic of the algorithm applied to derive the DCE grid, including two iterative edge-detection loops used to compute the DCE of open (red loop) and canopy (blue loop) pixels. Each iteration starts with a binary canopy mask B (1), which is smoothed applying a 3×3 -m moving average filter (grid S , 2). Combining B and S into overlay grids X (3) delineates open (red loop) and canopy pixels (blue loop) with a DCE corresponding to the iteration number N (4), and creates the binary input to the subsequent iteration step (5). Figure S1 in the supporting information visualizes the first three iteration steps of each loop.

validation points per plot. This was achieved by averaging the measurement at the intersection point and the four measurements surrounding it, where the intersection point was attributed double weight in the aggregation procedure. This strategy served to mimic the ALS sampling density, with each validation point representing a 1-m pixel. Validation points were matched to the nearest grid cell of the ALS-based snow depth map and classified into open outside-canopy (O) and under-canopy (C) locations. Snow depth averages and standard deviations were further computed at each plot, to allow a validation of aggregated

Table 2
Variables Aggregated to the Grid-Cell Level, With Associated Acronyms and Data Basis

Aggregated variable	Abbreviation	Data basis
Canopy and open fractions	CF, OF	Binary canopy mask
Class fractions based on distance to canopy edge (DCE)	D1F, D2F, D3F, D4F, D5F	DCE grid
Mean canopy height within canopy fraction	CH _{CF}	CHM, binary canopy mask
Mean-squared distance to canopy edge within open fraction	SDCE _{OF}	DCE grid, binary canopy mask
Standard deviation of DCE	STD _{DCE}	DCE grid
Mean snow depth	HS	HS grid
Mean snow depth within each DCE class	HS _{D1} , HS _{D2} , HS _{D3} , HS _{D4} , HS _{D5}	HS grid, DCE-based classification
Standard deviation of snow depth	STD _{HS}	HS grid
Snow-cover fraction	SCF	HS grid

snow depth descriptors relevant to our subsequent analysis. The match between ALS data and manual measurements was quantified in terms of root-mean-square deviation (RMSD), mean absolute deviation, and mean bias. To further verify the robustness of our results, we computed an additional HS map using the 17 May flight as the snow-off reference and repeated the evaluation. Validation plot locations were known to be snow free at this date based on local inspection.

Note that we do not offer a validation of the Grand Mesa data set, because it was separately evaluated in a concurrent study by Currier et al. (2019). Based on their results and the fact that the Grand Mesa data set was acquired with the same lidar setup and processed to the same standards, we assume this data set to be of very similar accuracy.

3.4. Data Aggregation to the Grid-Cell Level

ALS data were aggregated to grid cells with sizes spanning 1 order of magnitude, ranging from the size of our validation plots to typical resolutions of watershed- and regional-scale models (20, 50, 100, 200 m). A 50% overlap between neighboring grid cells was allowed in the aggregation procedure to optimize sample size. In the following, we use the term “pixel” to describe the 1-m units of the original gridded data sets, while the term “grid cell” is used to reference aggregated pixels.

The set of variables (Table 2) include grid-cell average quantities and subgrid variability metrics relating to both snow and canopy properties. These were derived from one or several 1-m resolution data sets presented in sections 4.1 and 3.3. Continuous variables (i.e., snow depth and DCE) were aggregated to averages and standard deviations. Class fractions of the various canopy categories were computed for each grid cell to characterize the arrangement of canopy elements within it, and snow depth averages specific to each canopy category were calculated. For instance, Dx_F (e.g., D1F) is the fraction of pixels in a grid cell classified as Dx (e.g., D1), and HS_{Dx} (e.g., HS_{D4}) the snow depth average of all pixels in a grid cell classified as Dx (e.g., D4).

Moreover, we defined three additional variables to characterize canopy density, the gap space, and overall canopy distribution within each grid cell. The average canopy height over the canopy pixels within each grid cell (CH_{CF}) is used as a proxy for vertical canopy density. In analogy, mean-squared distance to the canopy edge (SDCE_{OF}) serves to characterize gap area, and is calculated as the average of the squared DCE of open pixels within each grid cell. The overall canopy distribution is quantified by the standard deviation of DCE (STD_{DCE}), where a large STD_{DCE} implies that the grid cell contains areas of both dense canopy and larger gaps, while a small STD_{DCE} indicates the prevalence of one specific canopy class.

4. Results

4.1. Validation of ALS-Derived Snow Depth From the Swiss Data Set

Manually measured and ALS-based snow depths averaged over validation plots matched well between the two data sets (Bias: −4–0 cm, RMSD: 4–8 cm), and results were consistent even when using different summer scans as reference (Figure 4a versus 4b). Also, plot-scale standard deviations of snow depth conformed well with their respective validation data (Bias: 0–2 cm, RMSD: 2–3 cm), demonstrating that ALS accurately captured both the average conditions and the snow depth variability. Note, however, that snow depths derived from the first snow-on flight appeared to have a slightly larger bias than those derived from the second flight. This may be related to the limited number of snow-free pixels during the first flight, which are

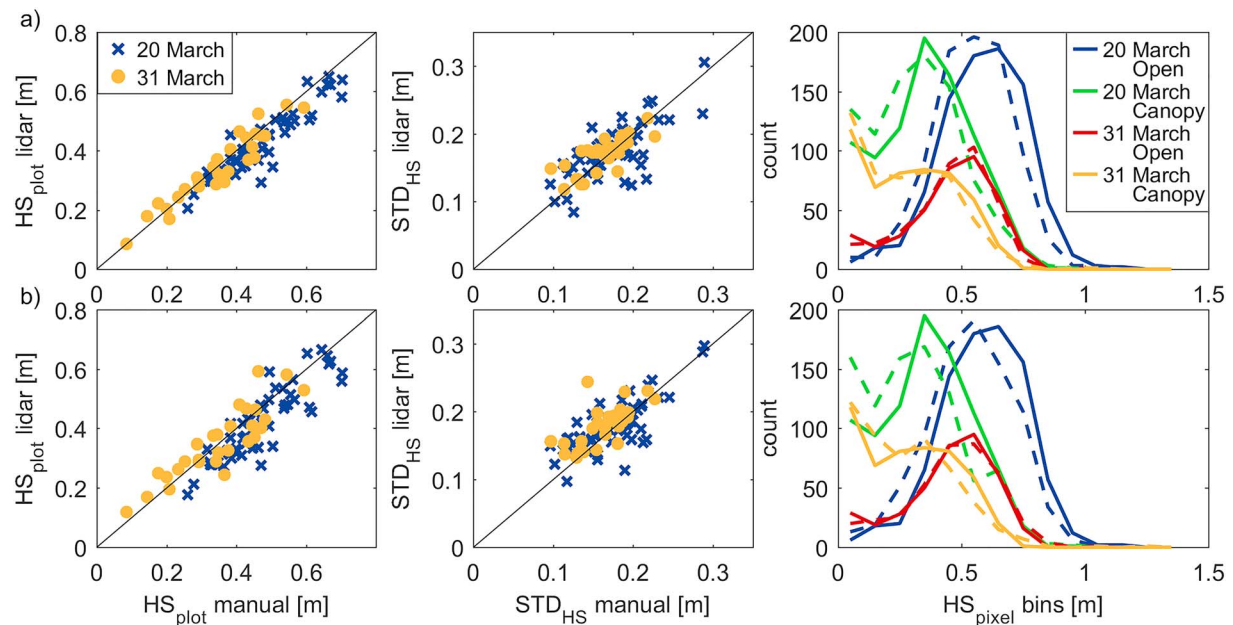


Figure 4. Comparison between (left) plot-scale snow depth mean and (middle) standard deviation from ALS-derived (1-m resolution) and manually surveyed snow depth. The right panels further show pixel-scale distributions of ALS-based (dashed lines) and in situ measured (full lines) snow depth, distinguishing canopy and open pixels. Data are shown for the flights on 20 and 31 March, using (a) the 17 May and (b) the 29 August reference snow-off scans.

routinely used to better register the snow-on and snow-off data to each other. Interestingly, high-resolution gridding was necessary to achieve the standard deviation observed from the manual measurements. An initial comparison to a 3-m resolution product derived by the standard ASO workflow (Painter et al., 2016) revealed consistently lower standard deviations than those computed from the 1-m HS map (cf. Text S2 in the supporting information).

At the pixel level (i.e., comparing individual manual validation points to ALS data at the 1-m scale), empirical distributions of snow depths computed over all validation plots were well reproduced by the ALS data (Figure 4, right). This applies to both under-canopy and outside-canopy regions, indicating that where ground returns could be identified, the data quality of canopy pixels was only slightly worse than that of open pixels (RMSD of 17–19 versus 10–13 cm, but equal bias of -5 – 0 cm). Detailed error statistics are available from Table S2 in the supporting information.

Snow depth patterns around trees varied greatly at our validation plots (20×20 m). Therefore, a qualitative comparison of different spatial patterns observed across the plots served to explore whether ALS succeeded in capturing this diversity. Figure 5 shows validation plots with a tree well (a), strong snow depth gradients (b), a rather homogeneous snow distribution (c), and partial snow cover (d). Overall, patterns captured by manual measurements were well reproduced by the ALS-based data sets, despite occasional discrepancies existing at individual points (cf. difference plots in Figure 5).

4.2. Relationships Between Snow Depth Distribution and Canopy Structure at the Pixel Level

Across each field area (Davos, Grand Mesa, Engadine), grouping pixels based on their DCE revealed a distinct relationship between snow distribution and pixel location relative to the surrounding canopy elements (Figure 6a). On average, lidar-based snow depths observed in under-canopy pixels were shallower and roughly constant for $DCE < -5$ m (i.e., within large canopy clusters). A pronounced increase in snow depth occurred over the transition from under-canopy to open ($-5 \text{ m} < DCE < 5 \text{ m}$) at all sites. For $DCE > 5$ m (i.e., further away from the canopy edge) snow depths approached a maximum (Grand Mesa) or a value close to the maximum (Swiss sites). Differential snow depth (Figure 6b) matched this trend in Grand Mesa, reflecting accumulation patterns from a snowfall between the two flights. Contrary, at the Swiss sites differential snow depth suggested highest depletion rates at outside-forest pixels, while these rates decreased as canopy density increased.

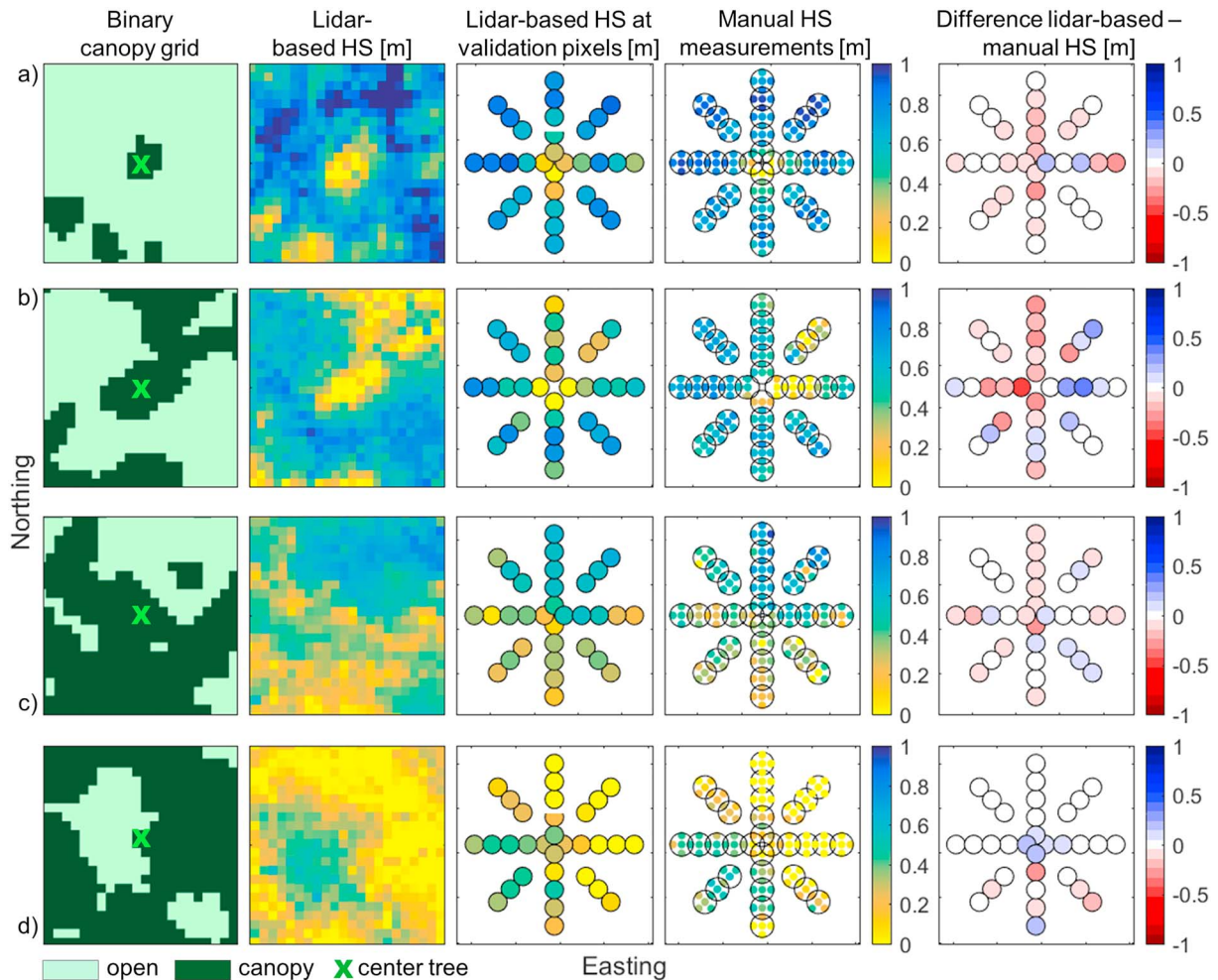


Figure 5. Spatial patterns at four different plots, featuring (a) a tree well, (b) a strong snow depth (HS) gradient, (c) a more homogeneous snow distribution, and (d) partial snow cover. Each panel shows a 25×25 -m area. Note that yellow in columns 2 to 4 represents 0 snow depth or no snow.

The consistent average behavior of snow depth around the canopy edge across sites and flight dates motivated DCE thresholds which we used to assign within-forest pixels to our five DCE-based classes (section 4.3 and Table 1). To this end, the thresholds were set to resolve the snow depth gradient around the canopy edge. Snow depth distributions within each DCE class are shown in Figure S5 in the supporting information. The upper limit of the “large gaps” class defined as 8 m away from the canopy implies that gaps with diameters of up to 16 m (i.e., on the order of one canopy height) fall within this class. This is in line with the 16-m scale break in snow depth distribution observed by Deems et al. (2006) and used by Broxton et al. (2015) to identify near-canopy pixels, and includes the majority of open pixels within the forest stand.

Empirical distributions of both absolute and differential snow depth in directional DCE classes disclose spatial snow cover dynamics within semiclosed forest (Figure 7). Both the Engadine and the Grand Mesa sites are reasonably flat, so snow distribution patterns evolve independent of local topographic or orographic effects. At the Engadine site, snow distribution at the onset of snowmelt (flight 1) is nearly identical on the north and south sides of the canopy edge (Figure 7a, left). But in line with data presented in Figure 6, considerable differences exist between the amount of snow under canopy and just outside the canopy. To the contrary, depletion rates feature reverse distribution characteristics. The south facing classes show higher depletion rates than the north facing classes, while differences in depletion rates just within and outside the canopy edge are minor for both orientations (Figure 7b, left). A spatial representation of this behavior (Figure 8) illustrates high depletion rates along exposed south facing canopy edges. Also, at Grand Mesa systematic differences exist in the distribution of snow across the forest edge (Figure 7a, right). The snowfall

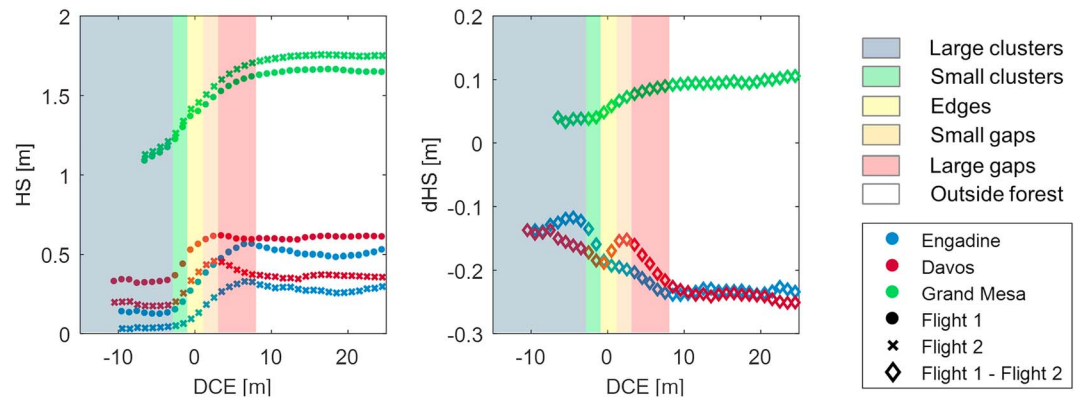


Figure 6. Relationships between (left) DCE and mean HS and (right) mean dHS over all pixels, background colors showing the DCE classes defined.

event captured between the two flights entails expected accumulation differences, with systematically less accumulation on the ground inside the canopy, while differences between directional classes are negligible (Figure 7b, right).

4.3. Relationships Between Snow Depth Distribution and Canopy Structure at the Grid-Cell Level

When aggregated over grid-cell domains, snow depth was stratified with DCE (Figure 9a). To demonstrate this, we determined mean snow depth within each of the five DCE classes separately (Table 2). Every single

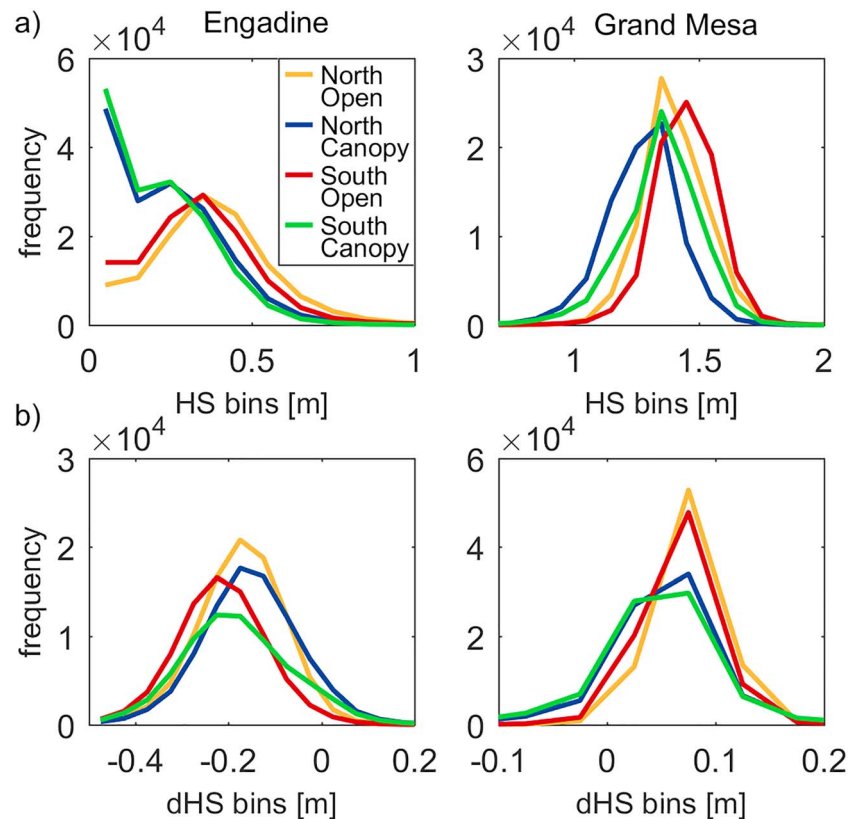


Figure 7. Empirical distributions of (a) snow depth (HS) from flight 1 and (b) differential snow depth between the two flights at the Engadine (left) and the Grand Mesa (right) sites, representing ablation and accumulation seasons, respectively. Histograms are specific to north and south facing edges, further discriminating between open and canopy pixels (cf. classifications in Table 1).

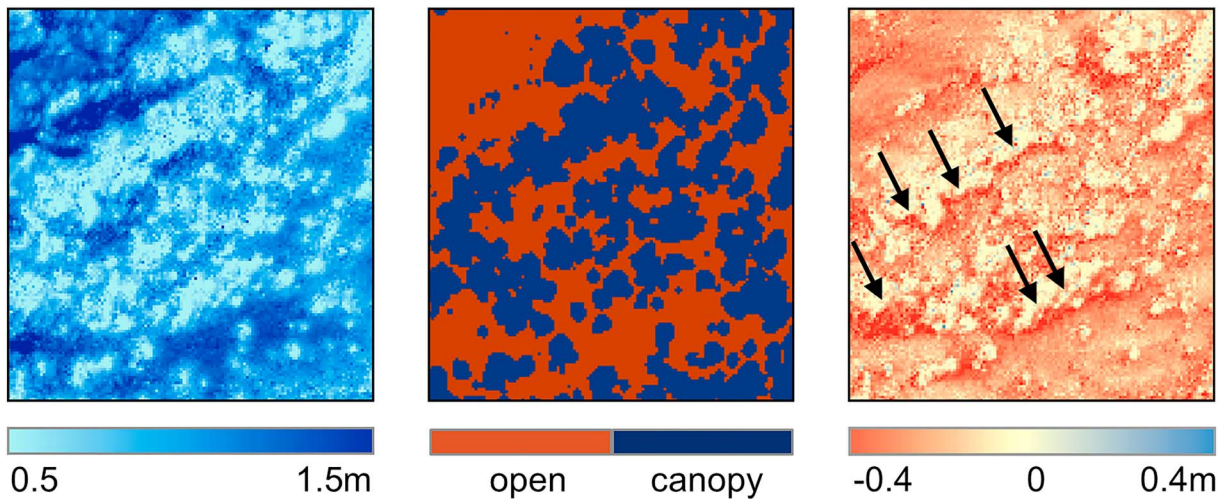


Figure 8. (left) Snow depth distribution from the first flight and (right) differential snow depth (20–31 March; i.e., melt period) together with the (middle) location of the canopy on a 100×120 -m area in the Engadine. The arrows point at areas featuring particularly high depletion rates, located to the south of canopy edges.

grid cell featured a remarkably consistent trend across DCE classes (Figure 9b), with less snow under dense canopy and more snow toward larger gaps. This effect was also consistent across all sites and all grid-cell sizes (Figure 9b). Yet individual grid cells show variable snow depths per DCE class. Not surprisingly, this variability impacts the overall mean snow depth per grid cell (cf. color scale in Figure 9a), such that individual grid cells with more snow per DCE class also feature an overall higher mean snow depth. The distribution of canopy classes across the grid cells was not able to explain the variability of snow depths per DCE class (data not shown), which suggests that other external factors, such as local precipitation gradients across the study area and/or topographic conditions, govern the overall snow input to the grid cell.

To remove possible influences of the above-mentioned external factors, we normalized each grid cell's mean snow depth (HS) by subtracting the mean snow depth of the center DCE class (HS_{D3F}). Normalized grid-cell average snow depth (nHS) exhibited a strong correlation to open fraction (OF) quantified by Pearson's R (Table 3), at all sites, for all flights, and all grid-cell resolutions, with the exception of large grid-cell resolutions (100–200 m) for the first flight in Davos. We found similar correlation statistics between nHS and mean-squared distance to the canopy edge ($SDCE_{OF}$), while correlations between nHS and mean canopy height (CH_{CF}) were comparably smaller and only strong for the Engadine site and large grid-cell resolutions.

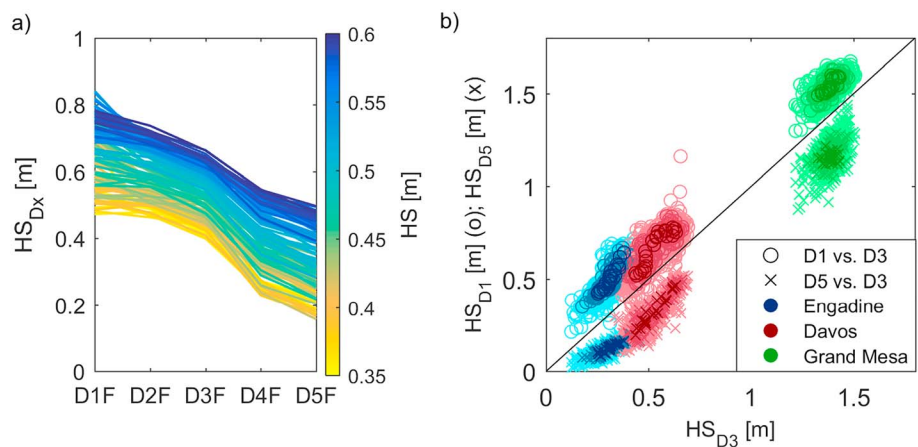


Figure 9. (a) Mean snow depth of each DCE class (HS_{Dx} , $x = 1, \dots, 5$) within 100-m grid cells for the flight on 20 March in Davos, where each line represents one grid cell connecting the associated HS_{Dx} values. The color scale shows the mean overall snow depth for each 100-m grid cell (HS). (b) Scatterplots between class-specific snow depth averages (edge class versus large gap class (o) and large cluster class (x), respectively), for the first flight at all sites and within grid cells of different resolutions (denoted by shading: light to dark: 50, 100, 200 m).

Table 3*Correlation Coefficients (Pearson's R) Between the Grid-Cell-Level Snow and Canopy Variables Mentioned in section 5.3, for All Sites and Grid-Cell Resolutions*

Correlated variables	Engadine				Davos				Grand Mesa			
	20 m	50 m	100 m	200 m	20 m	50 m	100 m	200 m	20 m	50 m	100 m	200 m
nHS _{F1} -OF	0.84	0.91	0.94	0.96	0.64	0.63	0.50	0.17	0.77	0.86	0.90	0.92
nHS _{F2} -OF	0.77	0.89	0.94	0.96	0.70	0.76	0.80	0.90	0.80	0.87	0.90	0.93
nHS _{F1} -SDCE _{OF}	0.76	0.79	0.82	0.78	0.47	0.34	0.22	-0.10	0.81	0.90	0.92	0.98
nHS _{F2} -SDCE _{OF}	0.70	0.73	0.79	0.72	0.57	0.52	0.58	0.72	0.84	0.91	0.93	0.98
nHS _{F1} -CH _{CF}	-0.59	-0.69	-0.80	-0.93	-0.06	0.06	0.10	0.10	-0.39	-0.24	-0.13	0.28
nHS _{F2} -CH _{CF}	-0.54	-0.66	-0.78	-0.92	0.05	0.22	0.40	0.70	-0.41	-0.26	-0.16	0.27
STD _{HS,F1} -STD _{DCE}	0.43	0.60	0.81	0.89	0.17	0.36	0.63	0.83	0.52	0.66	0.69	0.76
STD _{HS,F2} -STD _{DCE}	0.35	0.55	0.77	0.88	0.00	0.00	0.14	0.03	0.61	0.76	0.83	0.95

Subscripts F1 and F2 refer to the two flights, the prefix “n” to normalized variables.

The combined effect of open fraction and gap distribution characteristics is further illustrated in Figure 10. While the data confirm the strong correlation between nHS and the open fraction, the distribution of DCE classes within each grid cell also affects mean snow depth. For grid cells with equal open fraction (Figure 10a; x axis), average snow depth (y axis) increases with mean-squared distance to the canopy edge (color scale). Since SDCE_{OF} reflects typical gap size (section 4.4 and Table 2), the above finding suggests that for any given canopy cover fraction, mean snow depth is higher when the open fraction is concentrated in a few large gaps, and lower when the open fraction is the result of many fragmented small gaps.

The standard deviation of snow depth within a grid cell (STD_{HS}) quantifies overall subgrid variability. To quantify the level of heterogeneity of the canopy cover we considered the standard deviation of DCE within a grid cell (STD_{DCE}) and found remarkably high correlations between STD_{HS} and STD_{DCE} (Table 3), particularly at Grand Mesa and in the Engadine. Correlations were generally stronger for coarser grid resolutions, where subgrid variability is more relevant. A compilation of data from the first flight at all sites and for different spatial grid resolutions is available in Figures 11a and 11b.

An alternative way of characterizing canopy gap size distribution is to assess the ratio of large gaps relative to the total open fraction (D1F/OF), and the ratio of large tree clusters relative to the total canopy fraction (D5F/CF). In the parameter space defined by these two fractions, the standard deviation of snow depth (STD_{HS}) features a very distinct distribution (Figure 11c). The distribution suggests that the largest snow

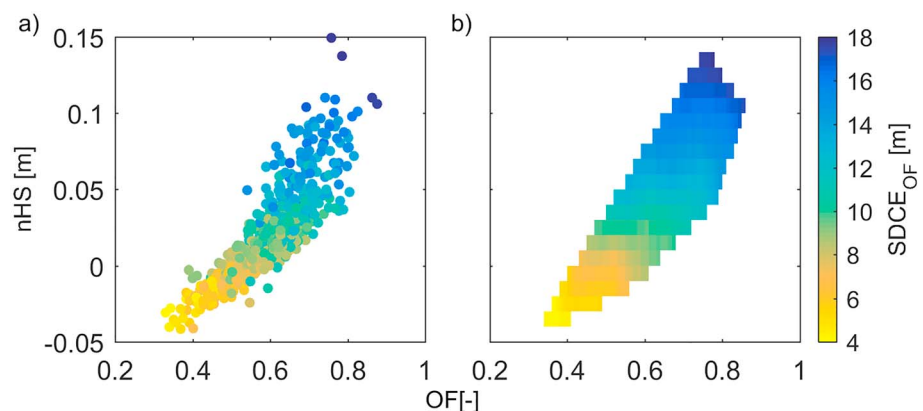


Figure 10. Relationship between open fraction (OF), normalized grid-cell average snow depth (nHS), and mean square distance to canopy edge (SDCE) illustrated (a) as scatterplot and (b) as interpolated surface. This example is based on data from the 16 February flight at Grand Mesa, 50-m grid-cell resolution.

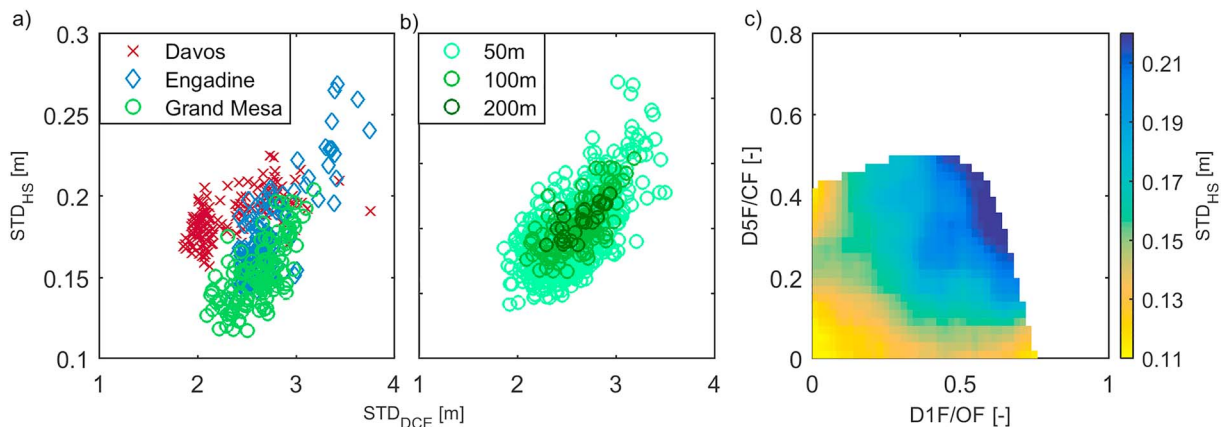


Figure 11. (a) Scatterplot of standard deviation of snow depth (y axis) and standard deviation of distance to canopy edge (x axis) within 100-m grid cells for the first flight at all sites and (b) within grid cells of different spatial grid resolutions for the Grand Mesa site. (c) Interpolated surface showing the dependence of standard deviation of snow depth (STD_{HS}) on large gap fraction relative to total open fraction ($D1F/OF$) and on large canopy cluster fraction relative to total canopy fraction ($D5F/CF$) for the Grand Mesa site.

depth variability is found in grid cells which include a mixture of both large gaps and dense canopy clusters, while the snow depth standard deviation is generally smaller if one or both of the extreme DCE classes (D1 and D5) is either prevalent or completely absent.

5. Discussion

5.1. Evaluation of Lidar-Derived Snow Depth Data Sets Within Forest Stands

At the pixel level, discrepancies between manual validation data and lidar-based snow depth maps identified at our sites were comparable to or smaller than what has been reported in previous studies on the performance of lidar in forests (Figure 4; Currier et al., 2019; Harpold, Gou et al., 2014; Hopkinson et al., 2004; Tinkham et al., 2014). Yet to our knowledge, this is the first study to evaluate mean and standard deviation of ALS-derived snow depth over forest plots, representing the grid-cell scale. As such, it approaches the validation from a novel perspective, focusing on the capability of ALS to capture spatial snow depth distributions in forest stands in general and around trees in particular. We acknowledge the potential error sources inherent to within-stand study sites (i.e., inaccuracies in the in situ data, misclassification errors, understory vegetation (Hopkinson et al., 2004; Hopkinson et al., 2012; Tinkham et al., 2014)), but demonstrated that these do not hinder a satisfactory representation of snow distribution patterns and their position relative to the canopy, both for under- and outside-canopy pixels (Figure 5). The minor impact of using two different summer scans, potentially confounded by the growth or decay of understory in between summer scans (Figure 4), further indicated that these patterns are comparably robust and insensitive to errors even at the scale of individual pixels. However, in accordance with observations by Tinkham et al. (2014) high-resolution (1 m) lidar data were required to resolve the observed spatial variability.

Based on these results, we could infer that both forest snow spatial patterns and distribution characteristics were reliably resolved in the ALS data sets. Demonstrating that ALS data sets can capture both between- and within-grid-cell variability was key to justifying the use of these data sets in the framework of a detailed forest snow variability analysis as presented in sections 5.2 and 4.3, especially at aggregated spatial scales. These findings further indicate that snow depth data sets obtained from airborne lidar can provide valuable validation data for testing forest snow models across larger spatial scales, a need identified in the forest snow model intercomparison project SnowMIP2 (Essery et al., 2009; Rutter et al., 2009).

Evaluating gap-filling approaches was beyond the scope of this study and unfeasible, as only very few manual validation points overlapped with areas where no ground returns could be identified. Even at the 1-m spatial scale, our data featured less than 10% gaps to be filled. However, Zheng et al. (2016) showed that interpolation can cause systematic overestimation of snow depth under trees when gaps are more prevalent (e.g., Harpold, Gou et al., 2014; Zheng et al., 2016). Interestingly, qualitative inspection of our data sets

indicated an increased occurrence of data gaps under dense spruce trees, the lower branches of which are often buried in the snow, supporting that accuracy may be species-dependent, as suggested by Hopkinson et al. (2004) and Tinkham et al. (2014). Steeper terrain slopes also appeared to be associated with larger data gaps. Results from this study may hence not be applicable to forests on steep slopes, and more research efforts are needed to evaluate the accuracy of lidar-based snow maps in forested, complex terrain.

The validation strategy deployed in this study did not allow us to assess the quality of the differential snow depth grids. Obviously, existing snow depth biases, albeit small, imply that the absolute magnitude of snow depth changes across the entire domain should be interpreted with caution. Nevertheless, the relative spatial patterns seen in the differential snow depth data appeared to be realistic from a process perspective; they reflect nonuniform accumulation, that is, resulting from snow interception by the canopy (e.g., Moeser, Stähli, et al., 2016), and enhanced snowmelt along Sun-exposed canopy edges (e.g., Veatch et al., 2009). Our confidence in the spatial patterns captured by the differential snow depth data was further increased by the remarkable representation of snow mobile tracks in an area adjacent to the Grand Mesa study sites (cf. Figure S6 in the supporting information). While not a major focus of this study, our results suggest that ALS-based differential snow depth data can be leveraged to gain new insights on snow accumulation and melt patterns in forest stands (see also Currier & Lundquist, 2018).

5.2. Canopy-Structure To Snow-Distribution Relationships in the Context of Experimental Studies and Forest Snow Modeling

Thanks to the spatial extent and coverage provided by today's ALS technology, co-located small-scale spatial snow and canopy distribution patterns within forest stands could be explored based on high-resolution, spatially complete data sets. Our findings corroborate the common observation that canopy gaps host more snow than under-canopy areas (Figure 6a) reported in many plot-scale studies based on high-resolution point measurements (e.g., Dickerson-Lange et al., 2015; Faria et al., 2000; Musselman et al., 2008) or terrestrial laser scans (Revuelto et al., 2015). But by leveraging the assets of the lidar-based data sets, we were able to assess the effects of small-scale snow distribution patterns across larger areas, and evaluate their impact at aggregated spatial scales, which had previously been hindered by the limitations inherent to deriving average snow depth estimates from point measurements (López-Moreno et al., 2011; Watson et al., 2006). Our analysis therefore complements the large body of literature concerned with snow variability within forest stands based on in situ data (cf. reviews by Clark et al., 2011; Lundquist et al., 2013; Varhola et al., 2010). Furthering work by Trujillo et al. (2007, 2009), who related the scaling behavior of within-stand snow depth fields to the scaling properties of the vegetation, we additionally assessed how these relationships could be used to describe grid-cell scale average snow depth and within-cell variability.

Repeated data acquisition captured an individual precipitation event at Grand Mesa and a 10-day snowmelt period at the Swiss sites. Observed links between snow distribution dynamics and canopy structure agreed well with prior studies concerned with accumulation (e.g., Dickerson-Lange et al., 2017; Moeser, Stähli, et al., 2016) and melt processes (López-Moreno & Latron, 2008; Musselman et al., 2012; Veatch et al., 2009). However, interception, unloading, wind-driven redistribution of snow, enhancement of longwave, and transmission of shortwave radiation all evolve and vary throughout the season and with meteorological conditions. We acknowledge that a targeted analysis at the level of individual processes would require periodic acquisitions at high temporal resolution. Emerging cheaper and flexible UAV-borne lidar systems (e.g., Almeida et al., 2019) however will likely facilitate more frequent surveys in the near future and help overcome limitations given by the small number of flights in our study.

The framework to characterize spatial arrangement of the canopy based on DCE offers a novel and continuous variable, applicable to both canopy and open pixels based on a simple, computationally efficient algorithm (available in the supporting information). While existing studies have attempted to relate snow depth to metrics such as tree size and spacing (Jost et al., 2007; Trujillo et al., 2007, 2009), or the distance from the stem (Faria et al., 2000; Musselman et al., 2008; Revuelto et al., 2015), highlighting the relevance of the canopy geometry, most canopy descriptors are applied to characterize either canopy pixels (e.g., the penetration fraction introduced by Zheng et al. (2016)) or the gap fraction within a forest stand (e.g., the total open area introduced by Moeser et al. (2015)). Alternatively, simple categorizations based on tree species (Faria et al., 2000) or discriminating between under-canopy and near-canopy pixels (Broxton et al., 2015) have been used, while Currier and Lundquist (2018) suggested a more detailed classification including canopy edges of

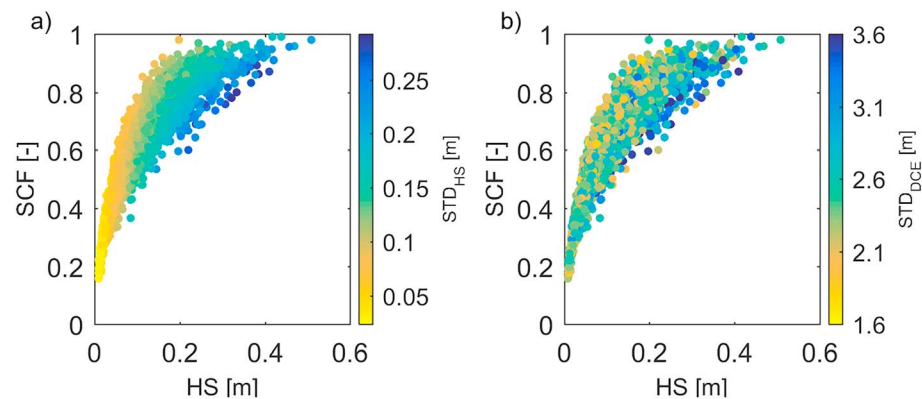


Figure 12. Snow-covered fraction (SCF; y axis) of 50-m grid cells at the Engadine site on 31 March as a function of grid-cell average snow depth (HS). Color scales illustrate (a) snow depth standard deviation and (b) standard deviation of DCE.

varying orientation, but focusing on larger-scale forest-structural features. Our approach builds upon these concepts, but enables additional flexibility, as it can be extended to directional variables, aggregated to any grid scale, and used to define canopy categories. As such, it is particularly suited to quantify within-stand, small-scale canopy heterogeneities, where different DCE-based variables could potentially be applied to describe individual processes (e.g., nondirectional variables for interception, directional variables for radiative transfer). Moreover, as DCE is evaluated from a binary canopy raster, it does not require canopy height information. Its applicability is therefore not limited to detailed lidar data, but extends to widely available aerial imagery, which implies that DCE-based canopy structure metrics can potentially be derived at near-global scale. On a standard personal computer, the DCE algorithm requires only about 3-s calculation time per km^2 grid for a canopy raster with a resolution of 1 m.

Many investigations of canopy-snow relationships, often in conjunction with topographic variables, have aimed to inform statistical modeling approaches (e.g., Tennant et al., 2017; Varhola et al., 2010; Zheng et al., 2016). However, we believe that canopy parameters correlated to snow depth across sites and at multiple points in time are also useful in view of upscaling physically based models. The consistent relationship between DCE-class specific snow depth averages within each grid cell (Figure 9) suggests a tiling approach based on these canopy categories as a possible implementation of subgrid heterogeneity within forest stands. This finding seconds model development efforts such as presented by Ellis et al. (2013) and Sun et al. (2018), who demonstrated how enhancing models to include the microclimates typical of forest gaps impacts snow accumulation, snowmelt timing, and runoff.

Moreover, the links between DCE-based metrics, grid-cell average, and standard deviation of snow depth (Figures 10 and 11) indicate that a PDF approach (Clark et al., 2011; Liston, 2004; Luce & Tarboton, 2004) may provide a successful alternative to account for unresolved variability. Here a canopy structure parameter based on DCE could be integrated into PDF functions describing specific forest architectures (e.g., dense versus discontinuous forest stands). To illustrate a potential application, we consider snow-covered fraction during the second flight in the Engadine. In Figure 12a, snow-covered fraction is plotted against grid-averaged snow depth and colorized by grid-cell standard deviation of snow depth, confirming the important relationship between partial snow cover, average snow depth, and snow depth variability known from previous research (e.g., Essery & Pomeroy, 2004; Luce & Tarboton, 2004). Being able to narrow down a generalized form of the depletion curve by way of a specific variable (here STD_{HS}) is a valuable asset of distributed models run over heterogeneous grid cells. STD_{HS} is not a standard output of land-surface models that include forest-snow processes, but as it is well correlated with the standard deviation of DCE, the former could be substituted with the latter to arrive at a similar characterization of the depletion dynamics (Figure 12b). Using STD_{DCE} instead of STD_{HS} offers the advantage of a predefined canopy metric of each grid cell, while tracking a meaningful STD_{HS} may be not as straightforward. Such a parameterization has, to our knowledge, not been attempted to date, but experimental data presented by Dickerson-Lange et al. (2015) corroborate its potential to predict fractional snow cover within forest stands.

Generally, strong correlations between canopy structure parameters and snow variables were observed for the Engadine and the Grand Mesa sites, demonstrating their validity at different geographic settings. These sites are reasonably flat, allowing snow dynamics to evolve independent of local topographic effects. The Davos site features more complex topography, and the correlations summarized in Table 3 are weaker. At this site, local microtopography and ground roughness (boulders, fallen logs, buried understory vegetation) may have masked canopy-induced snow distribution patterns (Watson et al., 2006; Winkler & Moore, 2006). Moreover, Clark et al. (2011) and Zheng et al. (2016) noted that larger-scale topography may even outweigh the impact of smaller-scale forest heterogeneity on snow distribution. But more research is required to quantify the interplay between large-scale topography, microtopography, and canopy structure, so that we can understand their combined impact on snow distribution at the grid-cell scale. In view of model applications, assessing the relevance of small-scale canopy heterogeneity is particularly interesting for regions like the European Alps or the Pacific Northwest, where the majority of forests reside in complex, rough terrain.

6. Conclusion

Based on high-resolution ALS data from NASA's 2017 SnowEx campaign at Grand Mesa, CO, and an equivalent data set acquired in the Eastern Swiss Alps in the same year, this study has demonstrated the capability of an ALS system to reliably capture high-resolution spatial snow distribution patterns within forest stands, as well as plot-scale snow depth averages and standard deviations. A novel, computationally efficient algorithm was applied to the same data sets to derive DCE, a spatially continuous canopy metric. This DCE metric can be aggregated to obtain meaningful nondirectional and directional canopy structure parameters that characterize grid cells of watershed and regional models. This approach allowed a detailed analysis of co-located canopy and snow distribution data within forest stands across spatial scales ranging from 1 to 200 m, in different geographic settings and during different times of the snow season.

At the pixel level (1-m scale), snow depth showed a very consistent relationship with DCE, with snow depth increasing along the gradient from dense canopy to the center of large canopy gaps. This effect generally outweighed differences between snow across forest edges of different orientation. Directional effects, however, appeared to become more prevalent during snowmelt. At the grid-cell level (20–200-m scale), average snow depths were strongly correlated to open fraction. Moreover, a DCE-based parameter quantifying gap size distribution accounted for differences in average snow depth between grid cells that feature the same canopy cover fractions. DCE was further successful in describing the standard deviation of snow depth within grid cells, particular for larger cells (≥ 50 m). This finding can be leveraged to describe snow depletion curves in forested environments in terms of the structural layout of the canopy.

Our results provide new evidence that dedicated structure parameters quantifying the spatial layout of canopy allow better representation of between- and within-cell snow variability than bulk parameters such as canopy cover fraction alone. Since these results were derived at the scale of typical grid cells in watershed and regional land surface models, and from observational data from two continents, concepts demonstrated here should be applicable to inform future model development. This could include large-scale models if the proposed DCE algorithm was applied to aerial imagery, which today is available almost globally.

Code and Data Availability

Data presented in this study are available from the WSL data repository Envidat (<https://www.envidat.ch/ui/#/metadata/als-based-snow-depth-and-canopy-height-maps-from-flights-in-2017-grisons-ch-and-grand-mesa-co>). The DCE algorithm code can be downloaded from <https://github.com/GiuliaMazzotti/DCE-algorithm>.

References

- Almeida, D. R. A., Broadbent, E. N., Zambrano, A. M. A., Wilkinson, B. E., Ferreira, M. E., Chazdon, R., et al. (2019). Monitoring the structure of forest restoration plantations with a drone-lidar system. *International Journal of Applied Earth Observation and Geoinformation*, 79, 192–198. <https://doi.org/10.1016/j.jag.2019.03.014>
- Andreadis, K. M., Storck, P., & Lettenmaier, D. P. (2009). Modeling snow accumulation and ablation processes in forested environments. *Water Resources Research*, 45, W05429. <https://doi.org/10.1029/2008WR007042>
- Bartlett, P. A., MacKay, M. D., & Versegny, D. L. (2006). Modified snow algorithms in the Canadian land surface scheme: Model runs and sensitivity analysis at three boreal forest stands. *Atmosphere-Ocean*, 44(3), 207–222. <https://doi.org/10.3137/ao.440301>

Acknowledgments

This project was funded by the Swiss National Science Foundation (SNF; project 625 169213). William Currier was funded by a NASA Earth and Space Sciences Fellowship, grant NNX16AO02H. Jessica Lundquist and Justin Pflug were supported by NASA grant NNX17AL59G. We would like to thank the ASO team, namely, Tom Painter, Kat Bormann, and Victoria Patterson, for their assistance in preparing and processing ALS point cloud data sets. Acquisition of manual validation data would not have been possible without an enormous team effort on the part of the SLF snow hydrology group, for which we thank Nena Griessinger, Nora Helbig, Clemens Hiller, Johanna Malle, Veronika Rieckh, Michel Schirmer, Constantin Vogt, Clare Webster, Adam Winstral, and Sebastian Würzer. We further acknowledge the help of Karl Steiner and Denis Vrabec with digitalizing field data, and the constructive comments of Sarah Barr on an initial draft of this manuscript. Finally, we thank three anonymous reviewers for their insightful comments and suggestions which improved the quality of this article.

- Best, M. J., Pryor, M., Clark, D. B., Rooney, G. G., Essery, R. L. H., Ménard, C. B., et al. (2011). The Joint UK Land Environment Simulator (JULES), model description: Part 1—Energy and water fluxes. *Geoscientific Model Development*, 4(3), 677–699. <https://doi.org/10.5194/gmd46772011>
- Bhardwaj, A., Sam, L., Bhardwaj, A., & Martín-Torres, F. J. (2016). LiDAR remote sensing of the cryosphere: Present applications and future prospects. *Remote Sensing of Environment*, 177, 125–143. <https://doi.org/10.1016/j.rse.2016.02.031>
- Biederman, J. A., Brooks, P. D., Harpold, A. A., Gochis, D. J., Gutmann, E., Reed, D. E., et al. (2014). Multiscale observations of snow accumulation and peak snowpack following widespread, insect-induced lodgepole pine mortality. *Ecohydrology*, 7(1), 150–162. <https://doi.org/10.1002/eco.1342>
- Bloeschl, G. (1999). Scaling issues in snow hydrology. *Hydrological Processes*, 13, 2149–2175. [https://doi.org/10.1002/\(SICI\)1099-1085\(199910\)13:14<2149::AID-HYP847>3.0.CO;2-8](https://doi.org/10.1002/(SICI)1099-1085(199910)13:14<2149::AID-HYP847>3.0.CO;2-8)
- Bonan, G. B., Patton, E. G., Harman, I. N., Oleson, K. W., Finnigan, J. J., Lu, Y., & Burakowski, E. A. (2018). Modeling canopy-induced turbulence in the Earth system: A unified parameterization of turbulent exchange within plant canopies and the roughness sublayer (CLM-ml v0). *Geoscientific Model Development*, 11(4), 1467–1496. <https://doi.org/10.5194/gmd-11-1467-2018>
- Boone, A., Samuelsson, P., Gollvik, S., Napoly, A., Jarlan, L., Brun, E., & Decharme, B. (2017). The interactions between soil–biosphere–atmosphere land surface model with a multi-energy balance (ISBA-MEB) option in SURFEXv8: Part 1—Model description. *Geoscientific Model Development*, 10(2), 843–872. <https://doi.org/10.5194/gmd-10-843-2017>
- Broxton, P. D., Harpold, A. A., Biederman, J. A., Troch, P. A., Molotch, N. P., & Brooks, P. D. (2015). Quantifying the effects of vegetation structure on snow accumulation and ablation in mixed-conifer forests. *Ecohydrology*, 8(6), 1073–1094. <https://doi.org/10.1002/eco.1565>
- Burles, K., & Boon, S. (2011). Snowmelt energy balance in a burned forest plot, Crowsnest Pass, Alberta, Canada. *Hydrological Processes*, 25(19), 3012–3029. <https://doi.org/10.1002/hyp.8067>
- Clark, M. P., Hendrikx, J., Slater, A. G., Kavetski, D., Anderson, B., Cullen, N. J., et al. (2011). Representing spatial variability of snow water equivalent in hydrologic and land-surface models: A review. *Water Resources Research*, 47, W07539. <https://doi.org/10.1029/2011WR010745>
- Currier, W. R., & Lundquist, J. (2018). Snow depth variability at the forest edge in multiple climates in the western United States. *Water Resources Research*, 54, 8773. <https://doi.org/10.1029/2018WR022553>
- Currier, W. R., Pflug, J., Mazzotti, G., Jonas, T., Deems, J., Bormann, K., et al. (2019). Comparing aerial lidar observations with terrestrial lidar and snow-probe transects from NASA's 2017 SnowEx campaign. *Water Resources Research*, 55. <https://doi.org/10.1029/2018WR024533>
- Deems, J. S., Fassnacht, S. R., & Elder, K. (2006). Fractal distribution of snow depth from lidar data. *Journal of Hydrometeorology*, 7(2), 285–297. <https://doi.org/10.1175/JHM487.1>
- Deems, J. S., Painter, T. H., & Finnegan, D. C. (2013). Lidar measurement of snow depth: A review. *Journal of Glaciology*, 59(215), 467–479. <https://doi.org/10.3189/2013JoG12J154>
- Dickerson-Lange, S., Lutz, J., Gersonde, R., Martin, K., Forsyth, J., & Lundquist, J. (2015). Observations of distributed snow depth and snow duration within diverse forest structures in a maritime mountain watershed. *Water Resources Research*, 51, 9353–9366. <https://doi.org/10.1002/2015WR017873>
- Dickerson-Lange, S. E., Gersonde, R. F., Hubbard, J. A., Link, T. E., Nolin, A. W., Perry, G. H., et al. (2017). Snow disappearance timing is dominated by forest effects on snow accumulation in warm winter climates of the Pacific Northwest, United States. *Hydrological Processes*, 31(10), 1846–1862. <https://doi.org/10.1002/hyp.11144>
- Ellis, C. R., Pomeroy, J. W., & Link, T. E. (2013). Modeling increases in snowmelt yield and desynchronization resulting from forest gap-thinning treatments in a northern mountain headwater basin. *Water Resources Research*, 49, 936–949. <https://doi.org/10.1002/wrcr.20089>
- Essery, R. L. H., & Pomeroy, J. W. (2004). Implications of spatial distributions of snow mass and melt rate for snow-cover depletion: Theoretical considerations. *Annals of Glaciology*, 38, 261–265. <https://doi.org/10.3189/172756404781815275>
- Essery, R. L. H., Rutter, N., Pomeroy, J. W., Baxter, R., Stähli, M., Gustafsson, D., et al. (2009). SnowMip2—An evaluation of forest snow process simulations. *Bulletin of the American Meteorological Society*, 90(8), 1120–1136. <https://doi.org/10.1175/2009BAMS2629.1>
- Faria, D. A., Pomeroy, J. W., & Essery, R. L. H. (2000). Effect of covariance between ablation and snow water equivalent on depletion of snow-covered area in a forest. *Hydrological Processes*, 14(15), 2683–2695. [https://doi.org/10.1002/1099-1085\(20001030\)14:15<2683::AID-HYP86>3.0.CO;2-N](https://doi.org/10.1002/1099-1085(20001030)14:15<2683::AID-HYP86>3.0.CO;2-N)
- Friesen, J., Lundquist, J., & van Stan, J. T. (2015). Evolution of forest precipitation water storage measurement methods. *Hydrological Processes*, 29(11), 2504–2520. <https://doi.org/10.1002/hyp.10376>
- Harpold, A. A., Biederman, J. A., Condon, K., Merino, M., Korgaonkar, Y., Nan, T., et al. (2014). Changes in snow accumulation and ablation following the Las Conchas Forest Fire, New Mexico, USA. *Ecohydrology*, 7(2), 440–452. <https://doi.org/10.1002/eco.1363>
- Harpold, A. A., Guo, Q., Molotch, N., Brooks, P. D., Bales, R., Fernandez-Diaz, J. C., et al. (2014). LiDAR-derived snowpack data sets from mixed conifer forests across the western United States. *Water Resources Research*, 50, 2749–2755. <https://doi.org/10.1002/2013WR013935>
- Harpold, A. A., Marshall, J. A., Lyon, S. W., Barnhart, T. B., Fisher, B. A., Donovan, M., et al. (2015). Laser vision: Lidar as a transformative tool to advance critical zone science. *Hydrology and Earth System Sciences*, 19(6), 2881–2897. <https://doi.org/10.5194/hess-19-2881-2015>
- Hodgson, M., Jensen, J., Raber, G., Tullis, J., Davis, B., Thompson, G., & Schmuckman, K. (2005). An evaluation of lidar-derived elevation and terrain slope in leaf-off conditions. *Photogrammetric Engineering and Remote Sensing*, 71(7), 817–823. <https://doi.org/10.14358/PERS.71.7.817>
- Hopkinson, C., Pomeroy, J. W., DeBeer, C., Ellis, C. R., & Anderson, A. (2012). Relationships between snowpack depth and primary LiDAR point cloud derivatives in a mountainous environment. *Proceedings of the Remote Sensing and Hydrology symposium*.
- Hopkinson, C., Sitar, M., Chasmer, L., & Treitz, P. (2004). Mapping snowpack depth beneath forest canopies using airborne lidar. *Photogrammetric Engineering and Remote Sensing*, 70(3), 323–330. <https://doi.org/10.14358/PERS.70.3.323>
- Jost, G., Weiler, M., Gluns, D. R., & Alila, Y. (2007). The influence of forest and topography on snow accumulation and melt at the watershed-scale. *Journal of Hydrology*, 347(1–2), 101–115. <https://doi.org/10.1016/j.jhydrol.2007.09.006>
- Khosravipour, A., Skidmore, A. K., Isenburg, M., Wang, T., & Hussin, Y. A. (2014). Generating pit-free canopy height models from airborne LiDAR. *Photogrammetric Engineering and Remote Sensing*, 80(9), 863–872. <https://doi.org/10.14358/PERS.80.9.863>
- Kim, E., Gatebe, C., Hall, D., Newlin, J., Misakonis, A., Elder, K., et al. (2017). NASA's SnowEx campaign: Observing seasonal snow in a forested environment. *Proceedings of the IEEE International Geoscience and Remote Sensing Symposium*. <https://doi.org/10.1109/IGARSS.2017.8127222>

- Liston, G. (1999). Interrelationships among Snow distribution, snowmelt, and snow cover depletion: Implications for atmospheric, hydrologic, and ecologic modeling. *Journal of Applied Meteorology*, 38(10), 1474–1487. [https://doi.org/10.1175/1520-0450\(1999\)038<1474:IASDSA>2.0.CO;2](https://doi.org/10.1175/1520-0450(1999)038<1474:IASDSA>2.0.CO;2)
- Liston, G. (2004). Representing subgrid snow cover heterogeneities in regional and global models. *Journal of Climate*, 17, 1381–1395. [https://doi.org/10.1175/1520-0442\(2004\)017<1381:RSSCHI>2.0.CO;2](https://doi.org/10.1175/1520-0442(2004)017<1381:RSSCHI>2.0.CO;2)
- López-Moreno, J. I., Fassnacht, S. R., Beguería, S., & Latron, J. B. P. (2011). Variability of snow depth at the plot scale: Implications for mean depth estimation and sampling strategies. *The Cryosphere*, 5(3), 617–629. <https://doi.org/10.5194/tc-5-617-2011>
- López-Moreno, J. I. & Latron, J. B. P. (2008). Influence of canopy density on snow distribution in a temperate mountain range. *Hydrological Processes*, 22(1), 117–126. <https://doi.org/10.1002/hyp.6572>
- Luce, C. H., & Tarboton, D. G. (2004). The application of depletion curves for parameterization of subgrid variability of snow. *Hydrological Processes*, 18(8), 1409–1422. <https://doi.org/10.1002/hyp.1420>
- Lundquist, J. D., Dickerson-Lange, S. E., Lutz, J. A., & Cristea, N. C. (2013). Lower forest density enhances snow retention in regions with warmer winters: A global framework developed from plot-scale observations and modeling. *Water Resources Research*, 49, 6356–6370. <https://doi.org/10.1002/wrcr.20504>
- Moesser, D., Mazzotti, G., Helbig, N., & Jonas, T. (2016). Representing spatial variability of forest snow: Implementation of a new interception model. *Water Resources Research*, 52, 1208–1226. <https://doi.org/10.1002/2015WR017961>
- Moesser, D., Morsdorf, F., & Jonas, T. (2015). Novel forest structure metrics from airborne LiDAR data for improved snow interception estimation. *Agricultural and Forest Meteorology*, 208, 40–49. <https://doi.org/10.1016/j.agrformet.2015.04.013>
- Moesser, D., Stähli, M., & Jonas, T. (2016). Improved snow interception modeling using canopy parameters derived from airborne LiDAR data. *Water Resources Research*, 51, 5041–5059. <https://doi.org/10.1002/2014WR016724>
- Murray, C. D., & Buttle, J. M. (2003). Impacts of clearcut harvesting on snow accumulation and melt in a northern hardwood forest. *Journal of Hydrology*, 271(1–4), 197–212. [https://doi.org/10.1016/S0022-1694\(02\)000352-9](https://doi.org/10.1016/S0022-1694(02)000352-9)
- Musselman, K. N., Molotch, N. P., & Brooks, P. D. (2008). Effects of vegetation on snow accumulation and ablation in a mid-latitude sub-alpine forest. *Hydrological Processes*, 22(15), 2767–2776. <https://doi.org/10.1002/hyp.7050>
- Musselman, K. N., Molotch, N. P., Margulis, S. A., Kirchner, P. B., & Bales, R. C. (2012). Influence of canopy structure and direct beam solar irradiance on snowmelt rates in a mixed conifer forest. *Agricultural and Forest Meteorology*, 161, 46–56. <https://doi.org/10.1016/j.agrformet.2012.03.011>
- Musselman, K. N., Pomeroy, J. W., & Link, T. E. (2015). Variability in shortwave irradiance caused by forest gaps: Measurements, modelling, and implications for snow energetics. *Agricultural and Forest Meteorology*, 207, 69–82. <https://doi.org/10.1016/j.agrformet.2015.03.014>
- Nolin, A. (2010). Recent advances in remote sensing of seasonal snow. *Journal of Glaciology*, 56(200), 1141–1150. <https://doi.org/10.3189/002214311796406077>
- Painter, T. H., Berisford, D. F., Boardman, J. W., Bormann, K. J., Deems, J. S., Gehrke, F., et al. (2016). The Airborne Snow Observatory: Fusion of scanning lidar, imaging spectrometer, and physically-based modeling for mapping snow water equivalent and snow albedo. *Remote Sensing of Environment*, 184, 139–152. <https://doi.org/10.1016/j.rse.2016.06.018>
- Pomeroy, J. W., Gray, D. M., Hedstrom, N. R., & Janowicz, J. R. (2002). Prediction of seasonal snow accumulation in cold climate forests. *Hydrological Processes*, 16(18), 3543–3558. <https://doi.org/10.1002/hyp.1228>
- Reutebuch, S., McGaughey, R., Andersen, H.-E., & Carson, W. (2003). Accuracy of a high-resolution lidar terrain model under a conifer forest canopy. *Canadian Journal of Remote Sensing*, 29(5), 527–535. <https://doi.org/10.5589/m03-022>
- Revelto, J., López-Moreno, J. I., Azorin-Molina, C., & Vicente-Serrano, S. M. (2015). Canopy influence on snow depth distribution in a pine stand determined from terrestrial laser data. *Water Resources Research*, 51, 3476–3489. <https://doi.org/10.1002/2014WR016496>
- Rutter, N., Essery, R., Pomeroy, J., Altimir, N., Andreadis, K., Baker, I., et al. (2009). Evaluation of forest snow processes models (SnowMIP2). *Journal of Geophysical Research*, 114, D06111. <https://doi.org/10.1029/2008JD011063>
- Sicart, J. E., Pomeroy, J. W., Essery, R. L. H., & Bewley, D. (2006). Incoming longwave radiation to melting snow: Observations, sensitivity and estimation in Northern environments. *Hydrological Processes*, 20(17), 3697–3708. <https://doi.org/10.1002/hyp.6383>
- Storck, P., Lettenmaier, D. P., & Bolton, S. M. (2002). Measurement of snow interception and canopy effects on snow accumulation and melt in a mountainous maritime climate, Oregon, United States. *Water Resources Research*, 38(11), 1223. <https://doi.org/10.1029/2002WR001281>
- Sun, N., Wigmosta, M., Zhou, T., Lundquist, J., Dickerson-Lange, S., & Cristea, N. (2018). Evaluating the functionality and streamflow impacts of explicitly modelling forest-snow interactions and canopy gaps in a distributed hydrologic model. *Hydrological Processes*, 32(13), 2128–2140. <https://doi.org/10.1002/hyp.13150>
- Tennant, C. J., Harpold, A. A., Lohse, K. A., Godsey, S. E., Crosby, B. T., Larsen, L. G., et al. (2017). Regional sensitivities of seasonal snowpack to elevation, aspect, and vegetation cover in western North America. *Water Resources Research*, 53, 6908–6926. <https://doi.org/10.1002/2016WR019374>
- Tinkham, W. T., Smith, A. M. S., Marshall, H.-P., Link, T. E., Falkowski, M. J., & Winstral, A. H. (2014). Quantifying spatial distribution of snow depth errors from LiDAR using random forest. *Remote Sensing of Environment*, 141, 105–115. <https://doi.org/10.1016/j.rse.2013.10.021>
- Toure, A. M., Luo, J., Rodell, M., Beaudoin, H., & Getirana, A. (2018). Evaluation of simulated snow and snowmelt timing in the Community Land Model using satellite-based products and streamflow observations. *Journal of Advances in Modeling Earth Systems*, 10, 2933–2951. <https://doi.org/10.1029/2018MS001389>
- Troendle, C. A., & King, R. M. (1987). The effect of partial and clearcutting on streamflow at Deadhorse Creek, Colorado. *Journal of Hydrology*, 90(1–2), 145–157. [https://doi.org/10.1016/0022-1694\(87\)90177-6](https://doi.org/10.1016/0022-1694(87)90177-6)
- Trujillo, E., Ramirez, J. A., & Elder, K. J. (2007). Topographic, meteorologic, and canopy controls on the scaling characteristics of the spatial distribution of snow depth fields. *Water Resources Research*, 43, W07409. <https://doi.org/10.1029/2006WR005317>
- Trujillo, E., Ramirez, J. A., & Elder, K. J. (2009). Scaling properties and spatial organization of snow depth fields in sub-alpine forest and alpine tundra. *Hydrological Processes*, 23(11), 1575–1590. <https://doi.org/10.1002/hyp.7270>
- Varhola, A., Coops, N. C., Weiler, M., & Moore, R. D. (2010). Forest canopy effects on snow accumulation and ablation: An integrative review of empirical results. *Journal of Hydrology*, 392(3–4), 219–233. <https://doi.org/10.1016/j.jhydrol.2010.08.009>
- Veatch, W., Brooks, P. D., Gustafson, J. R., & Molotch, N. P. (2009). Quantifying the effects of forest canopy cover on net snow accumulation at a continental, mid-latitude site. *Ecohydrology*, 2(2), 115–128. <https://doi.org/10.1002/eco.45>

- Watson, F. G. R., Anderson, T. N., Newman, W. B., Alexander, S. E., & Garrott, R. A. (2006). Optimal sampling schemes for estimating mean snow water equivalents in stratified heterogeneous landscapes. *Journal of Hydrology*, 328(3-4), 432–452. <https://doi.org/10.1016/j.jhydrol.2005.12.032>
- Webster, C., Rutter, N., Zahner, F., & Jonas, T. (2016). Modeling subcanopy incoming longwave radiation to seasonal snow using air and tree trunk temperatures. *Journal of Geophysical Research: Atmospheres*, 121, 1220–1235. <https://doi.org/10.1002/2015JD024099>
- Winkler, R., Boon, S., Zimonick, B., & Spittlehouse, D. (2014). Snow accumulation and ablation response to changes in forest structure and snow surface albedo after attack by mountain pine beetle. *Hydrological Processes*, 28(2), 197–209. <https://doi.org/10.1002/hyp.9574>
- Winkler, R. D., & Moore, R. D. (2006). Variability in snow accumulation patterns within forest stands on the interior plateau of British Columbia, Canada. *Hydrological Processes*, 20(17), 3683–3695. <https://doi.org/10.1002/hyp.6382>
- Zheng, Z., Kirchner, P. B., & Bales, R. C. (2016). Topographic and vegetation effects on snow accumulation in the southern Sierra Nevada: A statistical summary from lidar data. *The Cryosphere*, 10(1), 257–269. <https://doi.org/10.5194/tc-10-257-2016>